

Exploring the Regime of Validity of Global Gyrokinetic Simulations with Spherical Tokamak Plasmas

Y. Ren¹, W. Wang¹, W. Guttenfelder¹, S.M. Kaye¹, S. Ethier¹, R.E. Bell¹, B.P. LeBlanc¹, E. Mazzucato¹, D.R. Smith², C.W. Domier³, H. Yuh⁴ and the NSTX-U Team

¹Princeton Plasma Physics Laboratory, Princeton, NJ 08543

²University of Wisconsin-Madison, Madison, WI, 53706

³University of California at Davis, Davis, CA 95616

⁴Nova Photonics, Inc., Princeton, NJ 08540

E-mail contact of main author: yren@pppl.gov

Abstract. Plasma turbulence is considered one of the main mechanisms for driving anomalous thermal transport in magnetic confinement fusion devices. Based on first-principle model, gradient-driven gyrokinetic simulations have often been used to explain turbulence-driven transport in present fusion devices, and in fact, many present predictive codes are based on the assumption that turbulence is gradient-driven. However, using the electrostatic global particle-in-cell Gyrokinetic Tokamak Simulation (GTS) code [W.X. Wang et al., Phys. Plasmas 17, 072511 (2010)], we will show that while global gradient-driven gyrokinetic simulations provide decent agreement in ion thermal transport with a set of NBI-heated NSTX [M. Ono et al., Nuclear Fusion 40, 557 (2000)] H-mode plasmas, they are not able to explain observed electron thermal transport variation in a set of RF-heated L-mode plasmas, where a factor of 2 decrease in electron heat flux is observed after the cessation of RF heating. Thus, identifying the regime of validity of the gradient-driven assumption is essential for first-principle gyrokinetic simulation. This understanding will help us more confidently predict the confinement performance of ITER and future magnetic confinement devices.

1. Introduction

Micro-turbulence is considered to be a major candidate in driving anomalous transport in fusion plasmas [1]. The long-wavelength (ion-scale) Ion Temperature Gradient (ITG) mode [2], Trapped Electron Mode (TEM) [3], Kinetic Ballooning Modes (KBMs) [4], micro-tearing (MT) mode [5-7] and the short-wavelength (electron-scale) Electron Temperature Gradient (ETG) mode [8,9] are well-known instabilities which could drive micro-turbulence in fusion plasmas. Due to the kinetic nature of these instabilities, first principle gyrokinetic simulations are usually used to assess the turbulence-driven transport, and simulation results were compared with experiments in transport levels [10], turbulence amplitudes [11] and more sophisticatedly turbulence cross-phase [12]. This validation process [13] is crucial since to achieve the prediction capability of the performance of future fusion devices, we have to demonstrate that first-principle gyrokinetic models, which many predictive codes are based on, can reproduce results from current fusion devices. Validation is also a two-way process, meaning that predictions from gyrokinetic simulations constantly inspire new experiments. Such a positive feedback between experiments and simulations is essential to improve theories and numerical codes so that predictive capabilities can be eventually achieved. Furthermore, the validation process can also inform us the regime of validity of present models, i.e. the parameter regime where the models can provide trust-worthy answers, which gives us confidence in using the models and clues to improve the models in different parametric regimes. Here in this paper, we present a validation exercise conducted for the electrostatic global δf Particle-In-Cell Gyrokinetic Tokamak Simulation (GTS) code [14] using real spherical tokamak plasma equilibria from National Spherical Torus eXperiment (NSTX) [15]. GTS simulations were carried out for both NSTX Radio-frequency (RF)-heated L-mode and Neutral Beam Injection (NBI)-heated H-mode plasmas, and the predicted turbulence thermal fluxes were compared with experimental values from power balance analysis using TRANSP code [16]. What we found is that GTS simulations are not able to

explain observed electron thermal transport variation in a set of NSTX RF-heated L-mode plasmas before and after RF-heating cessation, while GTS simulations of the NBI-heated H-mode plasma show decent agreement in the ion thermal transport with the experiment. The results from these numerical simulations together with electron-scale turbulence measurements [17,18] indicate that gradient-driven assumption (that transport coefficients are assumed to be functions of local mean thermodynamic quantities and their gradients) used in GTS simulations may not be valid in the reported RF-heated L-mode plasmas. While further investigations are required to fully understand this issue, the understanding will help us more confidently predict the confinement performance of ITER and other future magnetic confinement devices.

2. Gyrokinetic Tokamak Simulation (GTS) code

Since the main goal of this paper is to present a validation study of the GTS code using NSTX plasmas, here we provide a more detailed description of the GTS code. The GTS code is presently an electrostatic global δf Particle-In-Cell code, which solves modern gyrokinetic equation in the conservative form [19]:

$$\frac{\partial f_a}{\partial t} + \frac{1}{B^*} \nabla_Z \cdot (\vec{Z} B^* f_a) = \sum_b C[f_a, f_b]$$

where f_a is the particle gyro-center distribution function of species a , \vec{Z} denotes the 5D gyro-center phase space variables, \vec{Z} describes the drift orbit of the gyro-center in phase space, $B^* = B + (m_a v_{\parallel} / e_a) \vec{b} \cdot \nabla \times \vec{b}$ with $\vec{b} = \vec{B} / B$, v_{\parallel} , e_a and m_a as the parallel velocity, particle charge and mass, respectively, and $C[f_a, f_b]$ is the Coulomb collision operator. The GTS code has newly improved weight scheme ensuing phase space incompressibility and has full tokamak geometry and global simulation domain (without local ballooning approximation used in local flux-tube gyrokinetic simulations). The GTS code also has fully kinetic electrons with both trapped and passing electron dynamics. The collision operator used in the GTS code is linearized Fokker-Plank operator with particle, momentum and energy conservation for both electron-electron and ion-ion collisions, and Lorentz operator is used for electron-ion collisions. The GTS code also includes neoclassical physics self-consistently in turbulence simulations (due to the large separation between turbulence time-scale and collision time-scale, neoclassical transport fluxes are not calculated in the GTS code). Presently, the GTS code has only electrostatic capability (its implication on the results presented here will be discussed later in the paper) and the electromagnetic capability is being implemented based on an improved electromagnetic scheme [20].

3. Results

In order to explore the regime of validity of the GTS code, it was applied to two quite different NSTX plasmas: one is a RF-heated L-mode plasma (shot 140301) with $B_T=0.55$ T and $I_p=300$ kA and the other is a NBI-heated H-mode plasma (shot 141767) with $B_T=0.55$ T and I_p of about 1 MA. We note that both plasmas shows strong changes in electrons-scale turbulence (measured by a high-k scattering system [21]) due to either the controlled changes in auxiliary heating (shot 140301) or plasma current (shot 141767) (see Ref.'s [18,22] for more details). Particularly, for shot 140301, the change in electron-scale turbulence was observed to correlate with the RF cessation occurring at about $t=479.6$ ms [see Fig. 1(d)], and for shot 141767, the change in electron-scale turbulence was observed to be caused by a controlled I_p ramp-down from about 1.1 MA at $t=400$ ms to about 0.9 MA at $t=460$ ms [see Fig. 1(a)]. For each plasma, GTS simulations were carried out both before and after the

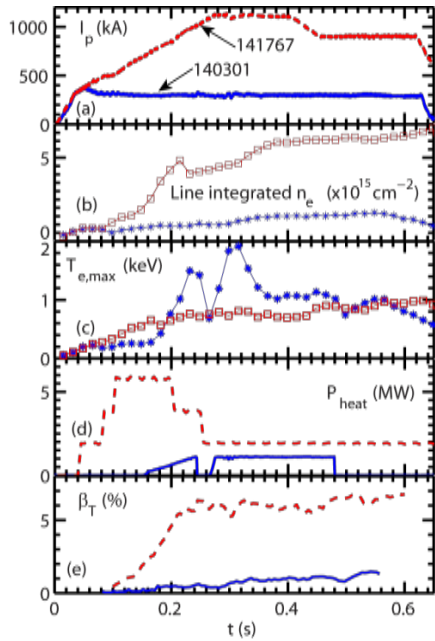


Figure 1 The time traces of plasma current, I_p , (a), line-integrated electron density (b), maximum electron temperature, $T_{e,max}$, (c), auxiliary heating power, P_{heat} , (d) and total toroidal beta, β_T , for shots 140301 [17,18] (blue) and 141767 (red). Different symbols are also used in (b) and (c): asterisks (140301) and open squares (141767). Solid and dashed lines are used for 140301 and 141767, respectively, in other panels. P_{heat} for shot 140301 denotes the injected RF heating power and for shot 141767, P_{heat} denotes the injected NBI-power. cessation of RF heating.

controlled changes, i.e. before ($t=465$ ms) and after ($t=482$ ms) the RF cessation for shot 140301, and before ($t=332$ ms) and after ($t=565$ ms) the current ramp-down for shot 141767. Since carrying out multi-scale global nonlinear simulations is prohibitively expensive with the present-day computational power, here we chose to focus on ion-scale simulation only. To provide some further comparisons between the two shots, we also note that while shot 140301 has higher or comparable maximum T_e compared with shot 141767 [Fig. 1(c)], shot 141767 has much higher line-integrated density (thus also higher β_T) than shot 141302 [Fig. 1(b) and Fig. 1(e)]. This higher β_T of shot 141767 may have implications for electron thermal transport, which will be discussed later in the paper.

Here we first present results from GTS simulations of shot 140301. Using global GTS simulations for this shot was motivated by the fact that local linear and nonlinear gyrokinetic simulations failed to explain observed fast response of electron-scale turbulence to auxiliary heating cessation and reduction in electron heat flux after the RF cessation in shot 140301 and other similar discharges [17,18] due to measured small changes in local equilibrium quantities in the turbulence measurement region before and after the RF cessation. Particularly, it was found in these RF-heated L-mode plasmas that, following the cessation of RF heating occurring in less than 200 μ s, a reduction in electron-scale turbulence spectral power was observed to occur on a time scale of 0.5-1 ms, much smaller than the energy confinement time of about 10 ms and a factor of 2 decrease in electron heat flux was inferred from power balance analysis after the

The choice of radial simulation domain for the GTS simulations is facilitated by local linear gyrokinetic stability analyses using the GS2 gyrokinetic code [23]. The GS2 code is an initial value gyrokinetic code which, in its linear mode, finds the fastest growing mode for a given pair of poloidal and radial wavenumbers. Figure 2 (a) shows the GS2-calculated ion-scale maximum linear growth rate, γ_{max} , real frequency at maximum linear growth rate, $\omega_{\gamma_{max}}$, and $E \times B$ shearing rate [24], $\gamma_{E \times B}$, at several radial locations for $t=482$ ms (after the RF cessation). It is clear that γ_{max} peaks around $R=135$ cm and drops substantially towards both the plasma core and edge. The real frequency of the most unstable mode goes from negative (electron drift direction) at $R \approx 130$ cm to positive (ion drift direction) at $R \approx 140$ cm, showing that there may be a transition from TEM-like mode to ITG-like mode. Further local linear stability analysis (not shown) for $R=135$ scanning normalized electron temperature gradient, a/L_{Te} , and normalized ion temperature gradient, a/L_{Ti} , (with β' fixed) shows that the ion-scale modes are actually driven unstable by both electron and ion temperature gradients (a is the half width of the last closed flux surface and β is the local plasma beta). $\gamma_{E \times B}$ can be seen to be close to zero, consistent with the small toroidal rotation observed in these RF-

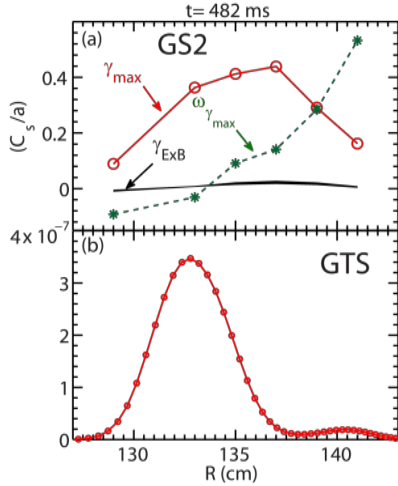


Figure 2 (a) Radial profiles of ion-scale maximum linear growth rate, γ_{\max} , (red open circle), real frequency at maximum linear growth rate, $\omega_{\gamma_{\max}}$, (green asterisks) and $E \times B$ shearing rate, $\gamma_{E \times B}$, (black band) for $t=482$ ms. Note that the vertical width of the black band denotes experimental uncertainties of $\gamma_{E \times B}$. (b) Turbulence intensity ($\propto \delta\psi^2$) profile during the linear phase of the GTS simulation, where $\delta\psi$ is the potential fluctuation.

heated plasmas, and is much smaller than γ_{\max} , which supports our approach of using nonlinear ion-scale simulations. The radial profile of γ_{\max} helped us to choose a radial domain from $\Psi_N=0.25$ to 0.8 ($R \sim 120$ cm to 147 cm) for global nonlinear GTS simulations, where Ψ_N is the square root of the normalized toroidal flux. The size of grids on poloidal planes is about local ρ_i , and 80 particles per cell-species were used. For comparison, the turbulence intensity ($\propto \delta\psi^2$, where $\delta\psi$ is the potential fluctuation) profile during the linear phase of the GTS simulation is shown in Fig. 2(b). Note that the fastest growing location in the GTS simulation is shifted towards the smaller radius compared with the radial profile of γ_{\max} in Fig. 2(a), showing that the quantitatively global effects make a difference even in linear phase.

In the GTS simulations, the experimental equilibrium $E \times B$ shear is turned on from the beginning (actually the $E \times B$ shear showed a small but destabilization effect, compared to the simulations without the $E \times B$ shear). Figure 3(a) compares electron energy flux, $Q_{e,GTS}$, radial profiles at $t=465$ (with RF heating) and 482 ms (after the RF cessation) from GTS simulations with those of the inferred electron heat flux, $Q_{e,exp}$. It can be clearly seen that while $Q_{e,GTS}$ is essentially the same for both $t=465$ ms and $t=482$ ms at $R \gtrsim 136$ cm, $Q_{e,GTS}$ at $R \lesssim 134$ cm is larger at $t=482$ ms than at $t=465$ ms. The observed change in $Q_{e,GTS}$ before and after the RF cessation is opposite to the change in experimental electron heat flux, $Q_{e,exp}$, from power balance analysis, in which $Q_{e,exp}$ at $t=465$ ms is about a factor of 2 higher than $Q_{e,exp}$ at $t=482$ ms. Furthermore, $Q_{e,GTS}$ at $t=465$ and 482 ms both show good agreement with $Q_{e,exp}$ at $t=482$ ms

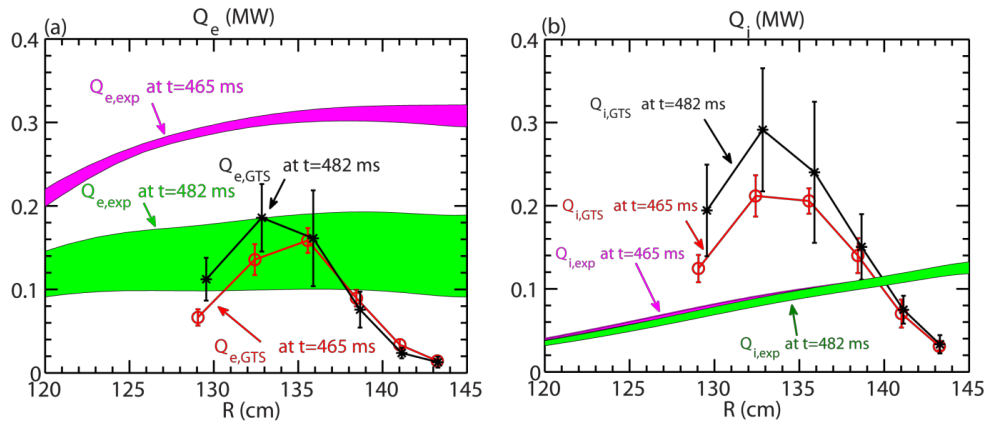


Figure 3 (a) Electron thermal transport: Red circles: electron energy flux, $Q_{e,GTS}$, at $t=465$ ms (before the RF cessation) as a function of major radius from nonlinear GTS simulation; black asterisks: $Q_{e,GTS}$ at $t=482$ ms (after the RF cessation) from nonlinear GTS simulation; magenta band: radial profile of experimental electron heat flux, $Q_{e,exp}$, at $t=465$ ms from power balance analysis; green band: radial profile of $Q_{e,exp}$ at $t=482$ ms. Note that the vertical widths of the magenta and green bands denote the experimental uncertainties. $Q_{e,GTS}$ is averaged over a quasi-steady saturation period, and the errorbars of $Q_{e,GTS}$ are the standard deviation of $Q_{e,GTS}$ in the averaging time period. (b) Ion thermal transport with the same denotations as in (a).

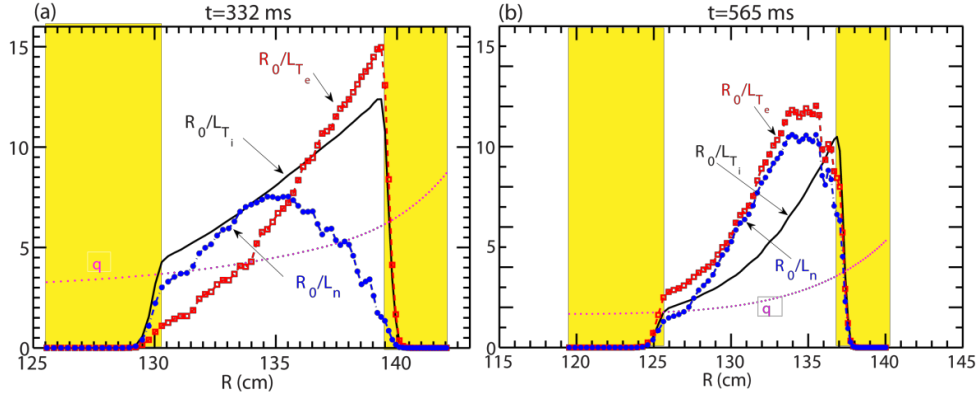


Figure 4 (a) Radial profiles of normalized equilibrium gradients and safety factor at $t=332$ ms: normalized electron temperature gradient, R_0/L_{T_e} (red open square), normalized electron density gradient, R_0/L_n (blue asterisks), normalized ion temperature gradient, R_0/L_{T_i} (black solid line) and safety factor, q (magenta dashed line). The simulation domain is from $\Psi_N=0.45$ to 0.9 ($R \approx 125.5$ cm to about 143.5 cm). (b) The same as (a) but for $t=565$ ms, except that the simulation domain is from $\Psi_N=0.25$ to 0.7 ($R \approx 119$ cm to about 140 cm). Note that R_0 is the major axis of the last closed flux surface. Also note that the yellow rectangles in (a) and (b) denote the buffer regions in the simulation and each has a width of $\Delta\Psi_N=0.1$.

for $R \lesssim 138$ cm but not with $Q_{e,\text{exp}}$ at $t=465$ ms when $Q_{e,\text{exp}}$ is about a factor of 2 higher due to the RF heating. We note that the decrease in $Q_{e,\text{exp}}$ towards larger radius at $R > 138$ cm is probably due to interactions with a buffer region from $R \approx 145$ to 147 cm and this will be investigated in future simulations with enlarged simulation domain. Predicted ion thermal transport is shown in Fig. 3(b), where changes in $Q_{i,\text{GTS}}$ between $t=465$ and 482 ms is seen to be similar to that of $Q_{e,\text{GTS}}$. However, the predicted $Q_{i,\text{GTS}}$ is significantly larger than $Q_{i,\text{GTS}}$ (which is essentially the same before and after the RF cessation) around $R=135$ cm, and the reason behind this is still under investigation. Similar as $Q_{e,\text{GTS}}$, $Q_{i,\text{GTS}}$ also decreases towards the boundary of the simulation domain and this issue will be addressed in the future together with $Q_{e,\text{GTS}}$ as discussed above. Nevertheless, these GTS simulation results are still consistent with previously-mentioned linear and nonlinear local electromagnetic gyrokinetic simulations (not shown) which showed that the observed equilibrium profile changes cannot explain the reduction in Q_e before and after the RF cessation [17,18]. The main reason behind this is that the observed equilibrium changes between $t=465$ and 482 ms were shown to be less than 15% around $R=135$ cm, and, unless the transport is very stiff (not supported by electron temperature gradient scans with local nonlinear simulations), gradient-driven simulations (both local and global) should show similar thermal transport. This is exactly what is seen in Fig. 3. Thus we conclude that global effects from profile variation, e.g. turbulence spreading, are not likely able to explain the observed reduction in electron thermal transport. These results imply that a nonlocal flux-driven mechanism like in Ref. [25] may be important for the observed electron thermal transport which is beyond the scope of fix-gradient simulation codes.

Having shown the gradient-driven GTS simulations were not able to account for the observed electron thermal transport variation associated with RF cessation in some RF-heated L-mode plasmas, here we show some good agreements in ion thermal transport between ion-scale GTS simulations and experiment in an NSTX NBI-heated H-mode plasma (shot 141767), where electron-scale turbulence was observed to be reduced/stabilized by an increase in electron density gradient induced by the controlled I_p ramp-down shown in Fig. 1(a) [22]. We focus on ion-scale simulation and apply the GTS code to two time points, i.e. before and after

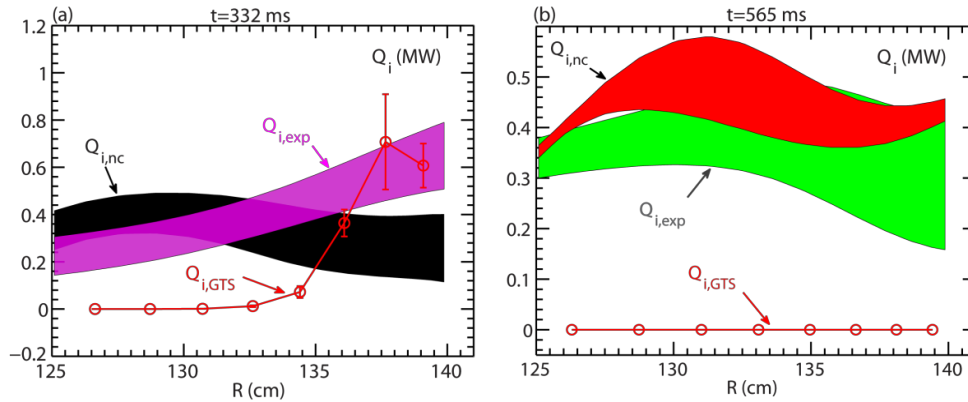


Figure 5 (a) Red circles: ion energy flux, $Q_{i,GTS}$, as a function of major radius from a nonlinear GTS simulation of shot 141767 at $t=332$ ms; magenta band: radial profile of experimental ion heat flux, $Q_{i,exp}$, at $t=332$ ms from power balance analysis; black band: radial profile of neoclassical ion heat flux, $Q_{i,nc}$. (b) Red circles: ion energy flux, $Q_{i,GTS}$, as a function of major radius from a nonlinear GTS simulation of the same shot but at a different time point of $t=565$ ms; green band: radial profile of experimental ion heat flux, $Q_{i,exp}$, at $t=565$ ms from power balance analysis; red band: radial profile of neoclassical ion heat flux, $Q_{i,nc}$. The same definition of uncertainties and errorbars applies for both (a) and (b) as in Fig. 3.

the I_p ramp-down as discussed previously. For these simulations, 40 particles per cell-species were used with the size of grids on poloidal planes is about local ρ_i . Figure 4 shows the simulations domains together with the radial profiles of some normalized equilibrium gradients and the safety factor, q , for $t=332$ ms and 565 ms. The simulation domains were chosen to cover a radial region with large core equilibrium gradients but to avoid the pedestal region where a δf code like GTS may have difficulty. It is clear that the normalized density gradient at $R=135$ cm becomes much large at $t=565$ ms than $t=332$ ms, consistent with the density profile steepening due to the I_p ramp-down, while the normalized ion temperature gradient become smaller at $t=565$ ms. We also note that since the current did not fully relax during the discharge, core q values continue to decrease.

Figure 5 compares the ion energy flux, $Q_{i,GTS}$, radial profiles at $t=332$ [Fig. 5 (a)] and 565 ms [Fig. 5 (b)] from the GTS simulation with those inferred from the experiment, along with

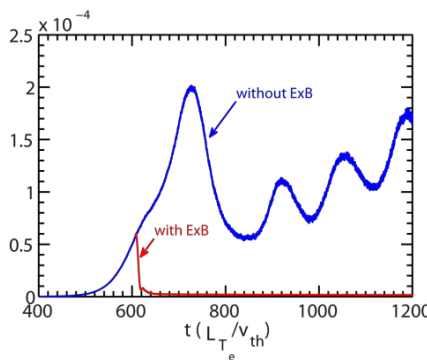


Figure 6 Time traces of turbulence intensity ($\propto \delta\psi^2$) at $R \approx 135$ cm from whole simulation domain [so $Q_{i,GTS}$ plotted as zero in Fig. 5 (b)]. However, this is still in agreement with the experiment, since $Q_{i,exp}$ is approximately equal to $Q_{i,nc}$, and turbulence-driven ion thermal transport is not needed. Thus we conclude that the GTS simulation results are in

good agreement in ion thermal transport with this and similar H-mode plasmas. However, from the GTS simulation for $t=565$ ms shown in Fig. 5(b) alone, we cannot tell the reason for the total suppression of ion-scale turbulence in the simulation. We note that for the GTS simulations shown in Fig. 5, the $E \times B$ shear is turned on from the beginning of the simulations. In order to assess the effects of the $E \times B$ shear, a GTS simulation without the $E \times B$ shear for $t=565$ ms was carried out. Figure 6 shows that without the $E \times B$ shear, the turbulence intensity (at $R \approx 135$ cm) grows nicely and reaches quasi-steady nonlinearly saturated state. However, in another GTS simulation with the $E \times B$ shear turned on during the simulation, the turbulence is almost immediately suppressed and remains at negligible levels for the remaining of the simulation as shown in Fig. 6. Thus the $E \times B$ shear is responsible for neoclassical level of ion thermal transport at $t=565$ ms, consistent with previous observations [27].

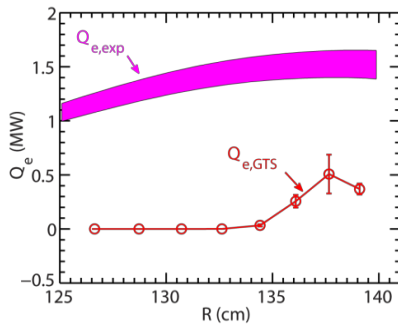


Figure 7 Red circles: electron energy flux, $Q_{e,GTS}$, as a function of major radius from a nonlinear GTS simulation of shot 141767 at $t=332$ ms; magenta band: radial profile of experimental electron heat flux, $Q_{e,exp}$, at $t=332$ ms from power balance analysis. The same definition of uncertainties and errorbars as in Fig. 3 also applies here.

The ion-scale turbulence in the GTS simulation for $t=332$ ms shown in Fig. 5(a) can also drive electron thermal transport, and its comparison with the experiment is shown in Fig. 7. It is clear that the predicted electron thermal transport, $Q_{e,GTS}$, is much smaller than the experimental value, $Q_{e,exp}$. As $t=565$ ms, since all ion scale turbulence is suppressed in the GTS simulation, the predicted electron thermal transport is zero as $Q_{i,GTS}$ shown in Fig. 5(b). We note that this shortfall in $Q_{e,GTS}$ compared with experimental values is not surprising since these ion-scale GTS simulations do not capture the residual ETG turbulence that may exist in the plasma. Furthermore, the GTS code is presently only electrostatic and does not include electromagnetic effects which may contribute to electron thermal transport. As shown in Fig. 1(e), shot 141767 has much higher β_T than shot 140301, and thus it is reasonable that electromagnetic effects may be more important for shot 141767 than for shot 140301.

4. Summary and discussion

In summary, global GTS simulations have been applied to two quite different NSTX plasmas, one NSTX RF-heated L-mode plasma and one NBI-heated H-mode plasma. In both plasmas, substantial turbulence variation was observed in correlation with controlled changes in experimental conditions, i.e. the RF heating cessation for the L-mode plasma and the I_p ramp-down for the H-mode plasma [18, 22]. Ion-scale GTS simulations before and after the changes in the experimental conditions for both plasmas were carried out in order to assess the simulation predictions in thermal transport against experimental values from transport analysis. It was found that for the L-mode plasma, while the GTS predicted electron thermal transport is in agreement with the experiment after the RF cessation, the GTS-predicted electron thermal transport before the RF cessation is about a factor of 2 smaller than the experimental level. Since the GTS code is gradient-driven and the measured equilibrium profile changes before and after the RF cessation are small, this discrepancy is not surprising, and this result is also supported by local linear and nonlinear gyrokinetic simulations [18]. Thus we conclude that the fixed-gradient GTS code is insufficient in explaining the observed changes in this and other similar RF-heated L-mode plasmas. A nonlocal flux-driven approach like in Ref. [25] may be needed. On the other hand, the GTS simulations applied to

the H-mode plasma reproduce quite nicely the observed change in ion thermal transport. However, the experimental electron thermal transport could not be explained by the ion-scale GTS, which is also not surprising since these GTS simulations did not have electron-scale resolution to capture the possible residual ETG turbulence in the plasma and no electromagnetic effects are presently implemented in the GTS code. Possibly, multi-scale interaction between ion-scale and electron-scale turbulence [28] may also play a role in explaining the discrepancies described above. In short, the fixed-gradient assumption of GTS code seems to be work better in NBI-heated H-mode plasmas than in certain RF-heated L-mode plasmas, although the fundamental reason behind this difference is still far from being understood. Future experiments on the recently commissioned NSTX-U [29] will help quantify the regime of validity of gradient-driven GTS simulations.

Acknowledgements: This work was supported by the U.S. Department of Energy under Contracts No. DE-AC02-76CH03073, No. DE-FG03-95ER54295, and No. DE-FG03-99ER54518. The computational resource for the GTS simulations was provided by the National Energy Research Scientific Computing Center.

References:

- [1] W. Tang, Nucl. Fusion 18, 1089 (1978)
- [2] B. Coppi and F. Pegoraro, Nucl. Fusion 17, 969 (1977)
- [3] B. Kadomtsev and O. Pogutse, Nucl. Fusion 11, 67 (1971)
- [4] W. Tang, J. Connor, and R. Hastie, Nucl. Fusion 20, 1439 (1980)
- [5] R. D. Hazeltine and H. R. Strauss, Phys. Rev. Lett. 37, 102 (1976),
- [6] J. F. Drake, N. T. Gladd, C. S. Liu, and C. L. Chang, Phys. Rev. Lett. 44, 994 (1980)
- [7] W. Guttenfelder et al., Phys. Rev. Lett. 106, 155004 (2011)
- [8] Y. C. Lee, J. Q. Dong, P. N. Guzdar, and C. S. Liu, Physics of Fluids 30, 1331 (1987)
- [9] W. Dorland, F. Jenko, M. Kotschenreuther, and B., Phys. Rev. Lett. 85, 5579 (2000)
- [10] Y. Ren et al., Physics of Plasmas 19, 056125 (2012)
- [11] L. Lin et al., Physics of Plasmas 16, 012502 (2009)
- [12] A.E. White et al., Physics of Plasmas 17, 056103 (2010)
- [13] P.W. Terry et al., Physics of Plasmas 15, 062503 (2008)
- [14] W.X. Wang et al., Physics of Plasmas 17, 072511 (2010)
- [15] M. Ono et al., Nuclear Fusion 40, 557 (2000)
- [16] R. J. Hawryluk, Physics of Plasma Close to Thermonuclear Conditions (Pergamon, New York, 1981)
- [17] Y. Ren et al., "Experimental Observation of Nonlocal Electron Thermal Transport in NSTX RF-heated L-mode plasmas", Proc. 25th Int'l. Atomic Energy Agency Fusion Energy Conference, EX/P6-43, St Petersburg, Russia Federation, October 13-18, 2014
- [18] Y. Ren et al., Phys. Plasmas 2, 110701 (2015)
- [19] W.X. Wang et al., Physics of Plasmas 22, 102509 (2015)
- [20] E.A. Startsev and W.W. Lee, Physics of Plasmas 21, 022505 (2014)
- [21] D. R. Smith et al., Rev. Sci. Instrum. 79, 123501 (2008)
- [22] J. Ruiz-Ruiz et al., Physics of Plasmas 22, 122501 (2015)
- [23] M. Kotschenreuther et al., Comp. Phys. Comm. 88, 128 (1995)
- [24] R. E. Waltz and R. L. Miller, Physics of Plasmas 6, 4265 (1999)
- [25] S.-I. Itoh and K. Itoh, Sci. Rep. 2, 860 (2012)
- [26] W.A. Houlberg et al., Phys. Plasmas 4, 3230 (1997)
- [27] S. M. Kaye et al., Nucl. Fusion 47, 499 (2007)
- [28] N. Howard et al., Nucl. Fusion 56, 014004 (2016)
- [29] J. Menard, et al., in Fusion Engineering (SOFE), 2011 IEEE/NPSS 24th Symposium on Fusion Energy (2011), pp. 1